Sādhanā (2023) 48:60
https://doi.org/10.1007/s12046-023-02113-3

Measurement and optimization of cutting forces, surface roughness and temperature in turning of AZ91 Mg alloy

MAHIR AKGÜN

Technical Sciences Vocational School, Aksaray University, Aksaray, Turkey
e-mail: mahirakgun@aksaray.edu.tr

MS received 19 April 2022; revised 20 October 2022; accepted 27 January 2023

Abstract. This study presents the experimental and statistical examination of machinability of AZ91 alloy, in terms of cutting forces (Fc, F*f*, and Fp), surface roughness (Ra) and cutting temperature (T). In the first step, test samples have been produced using the casting method and the microstructures of these samples have been characterized by SEM and EDS. Secondly, the turning tests have been performed in CNC turning at three different cutting speeds (200, 300, and 400 m/min), three different feed rates (0.1, 0.2, and 0.3 mm/rev), and three different depths of cut (1, 1.5, and 2 mm). Thereafter, the turning simulations have been performed by Deform 3D software. Finally, experiment results were statistically analyzed using Taguchi, Anova, and regression analysis. The outcomes of this study show that the feed rate is the most significant parameter with 69.43, 90.04, 88.53, and 96.22% effect rates on the cutting force components (Fc, Ff, and Fp) and surface roughness (Ra) respectively, while the cutting speed is the most significant parameter with 70.83% effect rates on the cutting temperature. There is an average of 4.5% deviation between the experimental and simulation results of Fc. The results also stated that the microstructure of the samples consisted of α-Mg phase and β-intermetallic (Mg17Al12) phase, and the built-up edge (BUE) formation was the dominant wear mode for all the cutting tools.

Keywords. AZ91 Mg alloy; machining; microstructure; surface roughness; cutting force; cutting temperature; optimization.

1. Introduction

Magnesium and its alloys have been widely used in weight-critical applications in the automotive, aerospace, and military industries due to their superior properties such as low density, high strength-weight rations, and excellent machinability. Apart from these properties, magnesium alloys have a relatively high coefficient of thermal expansion, thermal conductivity, specific heat, and relatively low electrical conductivity [1–3]. In our world, where global warming is felt more and more day by day, its usage area is increasing thanks to these properties because the lightness of magnesium alloys makes it important for many areas in terms of fuel economy and emission [4–6]. Automotive manufacturers have started short, medium, and long-term technology development studies in designing and producing parts with Mg alloys [7]. In the automotive sector, the reduction in weight, together with the use of innovative lightweight materials, including magnesium, provides fuel savings, and this has a significant effect on reducing CO_2 emissions, which is an essential indicator of environmental pollution [8]. Furthermore, Mg alloys are used as biodegradable implant materials in cardiovascular or orthopedics devices in the medical field due to their biocompatibility [9].

The machinability of Mg and its alloys is quite good in terms of important machinability performance indicators such as surface quality, cutting force, energy consumption and cutting temperature [10]. However, some limitations have been reported in the machining of Mg and its alloys. For example, Shi *et al* reported that adhesion, abrasion, and diffusion wear were dominant in the cutting tools in the milling of AZ91D magnesium alloy and these wear types adversely affected the surface quality [11]. In another study, Hou *et al* observed that chip ignition occurred when milling AM50A magnesium alloy [12]. The first preferred method to eliminate such problems is the use of cutting fluids, as they help reduce friction, increase heat transfer, and remove the formed chips from the cutting zone [13, 14]. Nevertheless, cutting fluids are difficult to use because of the chemical reactivity of magnesium with lubricants and the risk of ignition by small chips [15]. Dry machining can be used to overcome such problems. An optimum selection of machining parameters is required to ensure tolerance integrity and surface quality in dry machining as well. Although an operator obtains ideal

Published online: 06 April 2023

levels via experience or applied information, it is not easy to get a sustainable manufacturing process [16]. Therefore, the cutting efficiency can be increased by optimization and modelling the cutting parameters affecting the machining process.

The literature review focuses on the studies performed on the optimization and modelling of the cutting process in the machining of Mg alloys by metal-cutting methods. Kayır has performed a study on optimizing of cutting parameters in the drilling of AZ91 magnesium alloy [17]. He has reported that 0.3 mm/rev feed rate, 3000 rpm spindle speed and carbide tool are the suitable drilling parameters for diametral error, circularity error and surface roughness according to grey relational analysis. Vasu *et al* have examined the surface quality and cutting forces in machining of AZ91 alloy by grey relational analysis [18]. As a result, the authors indicated that the optimal combination for the minimum surface roughness and minimum cutting forces are as cutting tool edge (90°), cutting speed (270 m/min), and feed rate (F1) (0.04 mm/rev). *Shi et al* have investigated the tool wear behaviors in milling of AZ91D alloy [19]. They used the Taguchi method to analyze their test results. The results showed that the dominant wear models for carbide insert are adhesion wear, abrasion, and diffusion, and flank wear increased with an increase in cutting speed. Dey *et al* performed the optimization of input factors affecting output parameters in machining Al6061/cenosphere composite with electrical discharge machining (EDM) [20]. The outcomes indicated that the combination of the response surface methodology and grey relational analysis was successful in predicting performance characteristics (surface roughness, material removal rates, and electrode wear rates). Akyüz has investigated the effect of Al addition on the machinability of AZ series alloys regarding the surface roughness and the cutting forces [21]. He reported that the cutting force tended to decrease with the addition of 2% (mass ratio) Al to Mg. Chowdary *et al* have investigated the influence of heat treatment (at 410 °C for 6, 12, and 24 h) on the machinability and corrosion behavior of AZ91 alloy [22]. They reported that the machinability of AZ91 Mg alloy could be improved by developing supersaturated grains and reducing the amount of secondary phase.

The literature investigation showed that there are studies on the production, improvement of mechanical properties, and machining of AZ91 Mg alloy. However, it was observed that there is very limited work on the machining of this alloy and the surface quality, cutting temperate and cutting forces, which are important machinability criteria, are not modeled in the turning of the AZ91 alloy produced by the casting method. Hence, the main objective of this work is to investigate the influence of process parameters statistically and experimentally on the cutting force components (Fc, F*f*, and Fp), surface roughness and cutting temperature when turning AZ91 alloy.

2. Material and method

2.1 *Workpiece material*

The production of AZ91 magnesium alloys was carried out in an atmosphere-controlled 1200° C electric resistance furnace. Magnesium and its alloys (Al, Zn, Mn, Mg) are at a minimum purity of 99.9%. After the pure Mg together with Al alloying additions charged in the crucible melted, it was poured into molds made of hot work tool steel using a bottom casting system. During the melting process, shielding gas (Argon) is given to the furnace during the melting time to cut the contact of the environment where the casting will be made with the atmosphere.

In addition, Strontium (Sr) alkaline earth metal was used to cover the casting surface area and prevent oxidation. After the samples solidified in the mold, they were removed from the mold and subjected to homogenizing heat treatment (at 400 °C for 4 h) in graphite powder [23]. The result of elemental analysis of the samples made with the Spectrolab M8 optical emission spectrometer device is given in table 1. AZ91 magnesium alloy was produced using 182.6 gr Al, 15.6 Zn, 3.6 Mn, and 1800 gr Mg values in a 2000 gr alloy melting capacity melting pot. For the machinability tests, samples with a diameter of 50 mm and a length of 120 mm were produced. The porosities formed on the surfaces of the samples produced before the machinability tests were cleaned by removing 2 mm sawdust.

The SEM and EDS analyzes have been performed with a CARL ZEISS ULTRA PLUS GEMINI FESEM scanning electron microscopy (SEM) to define the morphology and composition of the samples. Hardness measurements were carried out by taking five hardness measurements on the SHIMADZU MCT-W tester using an HV0.5 (500g) load. The average of these five measurements shows the hardness value.

2.2 *Test procedure and measuring system*

The machining tests were carried out on an ALEX TECH ANL-75T, C-axis CNC turning machining center without coolant. The spindle motor power of the machine is 15 KW, and the spindle with variable stepless speed can reach the highest speed of 3500 rpm. In the experiments, coated carbide cutting tool is preferred in Kennametal's K313 grade and TCGT3252HP ISO designation. All cutting tool inserts have a nose radius of 0.8 mm. The experiments were also used a tool holder (TTJNR 2525M-16) with a 90° approach angle. A new insert has been used for each test.

Table 1. Chemical compositions of AZ91 alloy used in this research.

	Elements								
	Mg	Al	Zn	Mn	Si	Sn	Pb	Pr	Ce
Wt%	87.24	11.34	1.301	0.0043	0.848	0.0046	0.0022	<0.0005	<0.0015
	Ag	Ca	Zr	Fe	Ti	Cu	Nd	La	Y
	0.0004	0.0009	0.0046	0.0214	0.0017	<0.0002	<0.002	<0.001	<0.005

Table 2. Cutting parameters and levels.

		Level		
Symbol	Cutting parameters	I	II	III
Vc	Cutting speed (m/min)	200	300	400
f	Feed rate (mm/rev)	0.1	0.2	0.3
a	Depth of cut (mm)	1	1.5	2

The manufacturer's recommendations and the studies on magnesium alloys in the literature were considered while deciding the cutting parameters' levels. Table 2 shows the machining parameters.

Three components (Fc, F*f*, Fp) of the cutting forces have been measured using a Kistler 9257B type dynamometer and equipments. Figure 1 indicates the measurement system. At the same time, the cutting temperature occurring in each experiment was measured by using Flir brand 60 model thermal camera. Roughness measurements on the machined surfaces formed after each turning test were made with the Mitutoyo Surftest 211 Tester. In these measurements, the cut-off length and assessment length has been selected at 0.8 and 16 mm, respectively. Surface roughness measurements have been performed on three different surfaces by rotating workpiece 120° around itself parallel to its own axis after each measurement and the mean of the three measurements was taken as the Ra value of the workpiece. Furthermore, the tool wear mechanisms and types were examined via a Quanta FEG 250 scanning electron microscope (SEM).

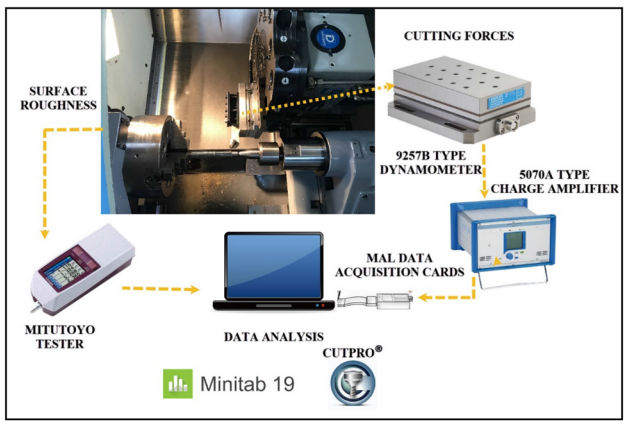

Figure 1. Schematic representation of the experimental setup.

2.3 *Experimental design and data analysis*

In recent years, it is seen that the use of optimization techniques in industrial areas has increased in many areas.

Especially, it is significant to define the ideal levels of the factors affecting a products development or make the production process more efficient. In the field of metal cutting, optimization techniques are also utilized to define the effect levels of the factors affecting the production process [24, 25]. One of these, the Taguchi method, is a process/product optimization method based on experiments planning, execution, and evaluation. In this context, the Taguchi method has been utilized in this study to describe the performances characteristic of control factors on output parameters. Turning experiments have been performed via the Taguchi L9 (3^3) orthogonal array. The "smaller-the-better" characteristic has been chosen because of desire to achieve the lowest levels of Fc, F*f*, Fp, and Ra. The S/N ratio of the "smaller-the-better" concept given in Eq. (1). Table 3 shows the test results.

$$n = \frac{S}{N} = -10\log\left(\frac{1}{n}\sum_{i=1}^{n} y_i^2\right) \quad (1)$$

Variance analysis (ANOVA) is applied to define the effect ratio of input factors on all outputs. The importance value (F) is considered in determining the effect levels of the factors and the magnitude of the F value indicates the level of influence of the factor on the results [26, 27]. The regression analysis has been also applied to state the relationship between cutting parameters and output parameters mathematically. The output factors are Fc, F*f*, Fp, Ra, and T, whereas the input factors are Vc (m/min), f (mm/rev), and ap (mm). Moreover, Taguchi-based gray relational analysis has been used to simultaneously identify an ideal combination of cutting conditions based on multiple output parameters. The application stages of Taguchi-based gray relational analysis are given in table 4. Lastly, confidence interval (CI) calculations were made for each output

Table 3. Experiment results.

	Parameters												
Test Id	A (V*c*)	B (*f*)	C (a)	Fc (N)	Fc-S/N (dB)	F*f* (N)	F*f*-S/N (dB)	Fp (N)	Fp-S/N (dB)	Ra (μm)	Ra-S/N (dB)	T (°C)	T-S/N (dB)
1	200	0.1	1	44.095	− 32.869	6.640	− 16.443	4.051	− 12.151	1.14	− 1.138	160	− 44.08
2	200	0.2	1.5	58.025	− 35.268	10.320	− 20.273	4.850	− 13.714	2.50	− 7.958	190	− 45.57
3	200	0.3	2	60.144	− 35.563	11.780	− 21.422	6.100	− 15.706	3.19	− 10.07	210	− 46.44
4	300	0.1	1.5	38.238	− 31.595	5.210	− 14.336	4.380	− 12.829	1.35	− 2.606	210	− 46.44
5	300	0.2	2	47.147	− 33.442	8.951	− 19.037	4.895	− 13.795	2.69	− 8.595	240	− 47.60
6	300	0.3	1	55.102	− 34.807	9.980	− 19.982	6.005	− 15.570	3.47	− 10.806	200	− 46.02
7	400	0.1	2	23.437	− 27.398	4.686	− 13.416	3.420	− 10.680	1.25	− 1.938	260	− 48.29
8	400	0.2	1	43.255	− 32.669	8.324	− 18.406	4.215	− 12.496	2.16	− 6.689	240	− 47.60
9	400	0.3	1.5	60.125	− 35.563	10.723	− 20.606	6.095	− 15.699	3.10	− 9.827	245	− 47.78

Table 4. Stages of the Taguchi-based GRA methodology.

Steps	Definitions and formulas
1	The reference sequence of length n is as follows $x_0 = (x_0(1), x_0(2), x_0(3), \ldots, x_0(n))$
2	Data Normalization; The smaller-the better $x_i(k) = \frac{\max x_i^0(k) - x_i^0(k)}{\max x_i^0(k) - \min x_i^0(k)}$
3	The gray relationship coefficient; $n\big(x_0(0), x_j(k)\big) = \frac{n_{min} + \zeta n_{max}}{n_{0i}(k) + \zeta n_{max}}$ ζε is a coefficient between (0,1). j=1, 2, … m; k= 1, 2, … n. The ζ function sets the difference between $n_{0i}(k)$ and n_{max}
4	Grey relational degree is calculated by equation; If impact on the performance of the output is equal; $\gamma(x_0, x_i) = \frac{1}{n}\sum_{n}^{k=1} n\big(x_0(k), x_j(k)\big)$ If impact on the performance of the output is not equal; $\gamma(x_0, x_i) = \frac{1}{n}\sum_{k=1}^{n} \varepsilon\big(x_0(k), x_j(k)\big)$ γ ranges from zero to one, 'n' is the number of performance measures.
5	Determination of the new levels of the input parameters
6	

parameter and the accuracy of the system was tested in optimum and random groups.

2.4 *Numerical analysis*

Deform 3D has been used for turning simulations. The operations performed during the simulation are explained in order. First, the workpiece material has been defined. The Johnson-Cook material model usually has been applied in the deformation testing methods. It is also widely used in the finite element analysis of the machining process, which is a high-strain deformation process [28]. In this context, Johnson-Cook material model constants, mechanical and physical properties are defined for AZ91 alloy in turning simulation. The constants used in the integration of the Johnson-Cook material model into the software are given in table 5 [29]. The mechanical and physical properties for the workpiece are also given in Table 6 [29, 30]. The Johnson-Cook material model is specified as:

$$\sigma^0 = (A + B(\varepsilon^p)^n)\left(1 + C\log\left(\frac{\dot{\varepsilon}^p}{\dot{\varepsilon}_0}\right)\right)\left(1 - \left(\frac{T - T_r}{T_m - T_r}\right)^m\right) \quad (2)$$

Table 5. Johnson–Cook parameters for the AZ91 alloy.

A (MPa)	B (MPa)	C	n
164	343	0.021	0.283
m	T_r (°C)	T_m (°C)	$\dot{\varepsilon}_0$
0	24	530	1

In this model, the hardening is a special type of isotropic hardening for which the yield stress is considered as σ^0 [31]. In Eq. (2), the symbols A, B, C, n, and m represents strain hardening, strain rate constant, strain hardening constant and thermal softening constant, respectively while the symbols $\dot{\varepsilon}_0$, ε^p, $\dot{\varepsilon}^p$, T, Tr, and Tm represents reference strain rate, plastic strain, plastic strain rate, reference temperature, room temperature, and melting temperature, respectively. At this stage, in addition to defining the workpiece material properties, the geometry information of the workpiece is also defined.

The length and height of workpiece model used were 5 mm and 1 mm, respectively. In the second step, the tool material and geometry have been defined. In the final step, turning simulations are performed for each process combination by defining the tool-workpiece interface friction coefficient (Coulomb friction accepted as 0.6) and the meshing parameters (0.1 and 0.02 mm for the maximum and minimum element size). Figure 2 shows the model scheme for turning simulations.

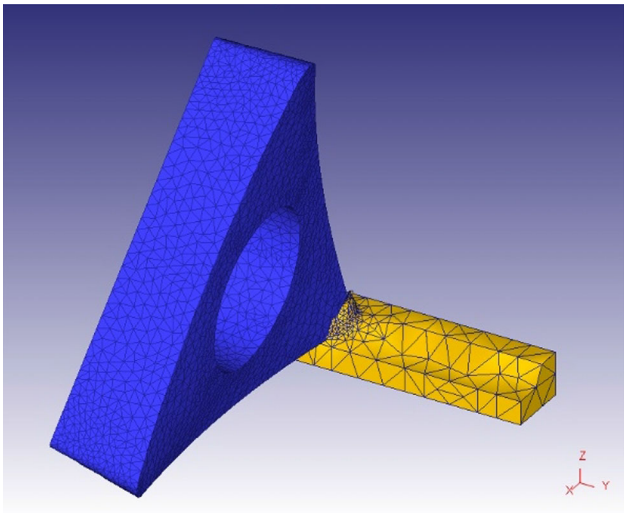

Figure 2. Mesh structure utilized for the simulation of the turning process.

3. Experimental Results and Analysis

3.1 *Microstructure and Hardness*

Figure 3 shows the SEM microstructure and EDS analysis results of the AZ91 alloy produced by the casting method. The EDS analysis was performed in the spectral points 1, 2, 3, 4, 5, 6, and 7 marked in the microstructure of the sample. When figure 3 is examined, it is seen that the microstructure of AZ91 alloy consists of α-Mg phase as well as β-intermetallic phase spread along grain boundaries. In the literature, precipitation of Al metal at the grain boundaries of Mg-Al binary alloys and the formation of phases such as $Mg_{17}Al_{12}$, Al_3Mg_2 and $Mg_{24}Al_{17}$ with different phase compositions in the β-intermetallic structure are expected [32–34]. β-phase ($Mg_{17}Al_{12}$) intermetallic compound was

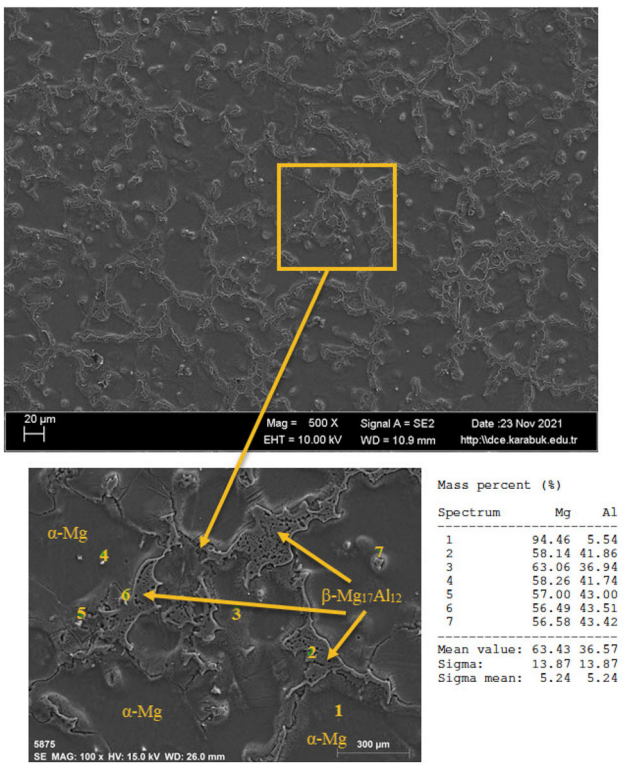

Figure 3. Microstructure images and EDS results of AZ91 magnesium alloy.

Table 6. Mechanical and physical properties of AZ 91.

Density (g/cm^3)	Poisson's ration	Young's Modulus (GPa)	Thermal Conductivity (W/mK)	Specific Heat (J/kg°C)
1.81	0.35	45	72.7	1.05

determined on the grain boundaries, and grain bodies as a result of SEM microstructure and EDS examinations. This situation can be explained by the decrease in the magnesium ratio and the increase in the aluminum ratio in other points compared to Point 1. Furthermore, according to the results of the element distribution analysis (EDS) for the AZ91 alloy, it was determined that Mg was homogeneously distributed in the structure and concentrated in the β-intermetallic phase of Al on the grain boundaries and grain bodies (figure 4). Similar results have been reported in the literature. For example, Liang *et al* in the microstructure evaluation of AZ91, reported that the β-intermetallic ($Mg_{17}Al_{12}$) phase spreads along the grain boundaries of the α-Mg matrix [35]. Similarly, Florina *et al* reported that the microstructure of as-cast AZ91 is composed of primary α-Mg as the matrix phase and the discontinuous and divorced $Mg_{17}Al_{12}$ phase [36]. On the other hand, the hardness of the produced sample was measured as 58.24±5 HV.

3.2 *Main cutting force (Fc)*

The main cutting force (Fc) values that are significant at the primary level regarding energy consumption and machine tool dynamics and design are evaluated more priority than other cutting force components in metal cutting processes. Figure 5 shows the variation of Fc depending on the input parameters. Where it is observed that an increase in Vc led to a decreasing trend in Fc. the Fc values is about 20–30% decrease with increasing Vc from 200 to 300 mm/min while about 10–15% decrease with increasing Vc from 300 to 400 m/min. This situation is consistent with the literature. In the literature, the decrease in Fc values with the increase in Vc can be explained by the decrease in the cutting strength of the material adhering to the tool-chip contact surface with the increase in the temperature in the cutting zone, and accordingly, the decrease in the tool-chip contact length [37, 38].

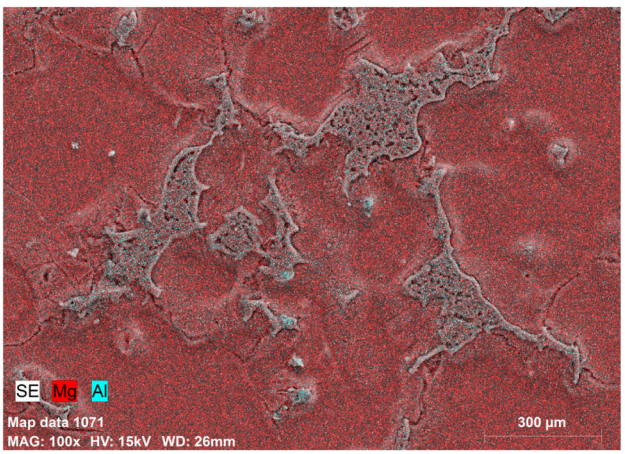

Figure 4. EDS maps images of AZ91 magnesium alloy.

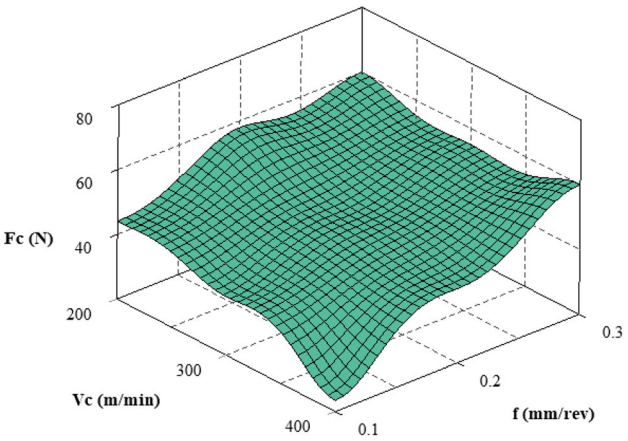

Figure 5. Fc assessment.

Fc was more affected by the change in feed rate than other cutting parameters. When figure 5 is examined, it is seen that Fc enters an increasing trend with the increase in the feed rate. Vasu *et al* reported that the high cutting forces occur with the increase of the feed rate in the machining of AZ91 alloy [39]. Moreover, they observed that the cutting forces decreased somewhat with the increase in cutting speed.

3.3 *Passive force (Fp)*

Figure 6 shows the change in passive force according to different cutting parameters. The passive force (Fp) values are generally accepted as the lowest of the cutting force components in machining, empirically and experimentally. The passive force measured in the turning test performed under all machining conditions are lower than the Fc and F*f*. Moreover, the passive force generally decreases by increasing Vc, like the main and feed forces. When figure 6

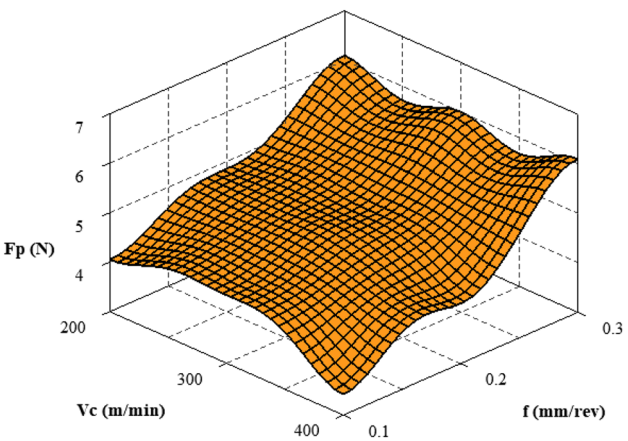

Figure 6. Fp assessment.

is examined, it is observed that the Fp values are about 10–15% decrease with increasing Vc from 200 to 300 m/min while about 20–25% reduction with increasing Vc from 300 to 400 m/min. However, the Fp values have about 30–35% rise with increasing *f* from 0.1 to 0.2 mm/rev while about 40–45% increase with increasing *f* from 0.2 to 0.3 mm/rev.

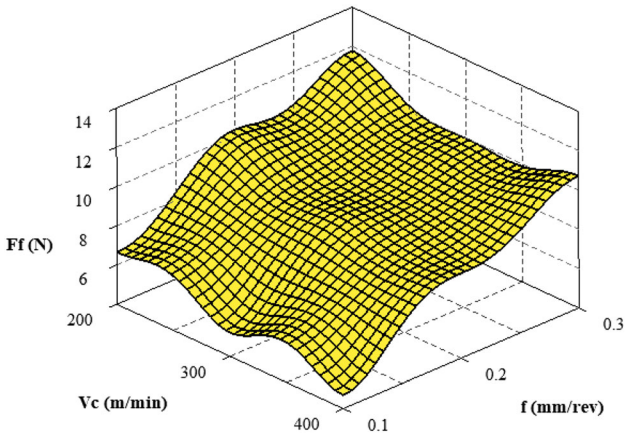

Figure 7. Ff assessment.

3.4 *Feed force (Ff)*

The feed force (F*f*) is of secondary importance among the cutting forces after the main cutting force in the turning operation, while it is of primary importance for the drilling operation.

The cutting tool geometry determines the magnitudes of the feed force and radial force components. The approach angle and the cutting tool nose radius are very effective on these components. Therefore, the cutting tool nose radius value has been considered in determining the depth of cut. The depth of cut values has been determined above the cutting tool tip radius value because ploughing effect can occur when the tool nose radius is higher than the depth of cut. Figure 7 shows the feed force (F*f*) variation graph measured in turning tests performed according to different cutting parameters. When figure 7 is examined, feed force shows a similar trend with Fc and Fp values. The highest feed force value has been obtained as 11.78 N in the turning test performed at 200 m/min, 0.3 mm/rev, and 2 mm depth of cut. While the feed force increases with increasing *f,* it decreases with increasing Vc. For example, the Ff values have about 40% increase with increasing *f* from 0.1 to 0.2 mm/rev while about 48–55% increase with increasing *f* from 0.2 to 0.3 mm/rev. At the same time, the Ff values is about 20–25% decrease with increasing Vc from 200 to 300 m/min while about 50–60% reduction with increasing Vc from 300 to 400 m/min. Figure 8 shows the images of

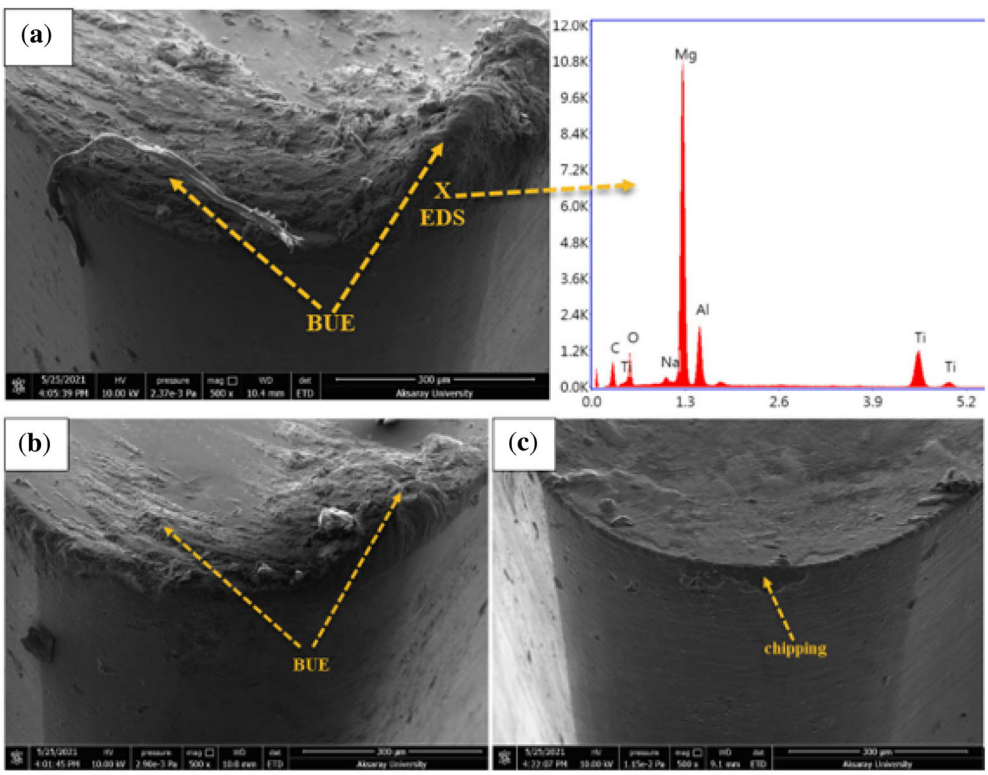

Figure 8. SEM images of the cutting tools after machining at 200 m/min, b 300 m/min, and c 400 n/min. (500X).

cutting tools created via SEM after experiments performed at all levels of cutting speed, 0.1 mm/rev feed rate, and 1 mm depth of cut. Considering the experimental results for Fc, Ff, and Fp, it is possible to say that the *f* (mm/rev) on the three cutting force components is more effective than the other cutting parameters and the ductility of AZ91 alloy is effective in the formation of the built-up edge (BUE) depending on the adhesion mechanism (figure 8). Moreover, looking at the images in figure 8, it is observed that extreme BUE formation takes shape with heavy adhesion because of the high ductility of the material in dry machining at low cutting speeds.

3.5 *Surface roughness (Ra)*

Figure 9 shows the influences of the cutting parameters on Ra. When figure 9 is examined, it is seen that the Ra value tends to reduce with the increase in the Vc, but the Ra values increase with increasing f (mm/rev) as expected for all Vc and a. Table 6 shows that the *f* has a significant influence on the surface roughness. Moreover, the Ra values have approximately 40–50% increase with increasing *f* from 0.1 to 0.2 mm/rev while approximately 60–65% increase with increasing *f* from 0.2 to 0.3 mm/rev. The Ra values have about 35–40% decrease with increasing Vc from 200 to 300 m/min, while about 50–60% decrease with increasing Vc from 300 to 400 m/min. The surface roughness is generally decreased due to decreasing the tendency of built-up edge (BUE) formation with increasing Vc has been reported by researchers [18, 41].

According to figure 8, the built-up edge (BUE) formation has occurred depending on the adhesion mechanism due to the high ductility of AZ91 alloy. When EDS analysis of the cutting tool used at 200 m/min has been examined, it is seen that diffusion of some elements (Mg, Al, C, Ti, Na) from the machined material to the cutting tool. Moreover, depending on the increase in Vc, the tendency of BUE formation decreases. This result may be also explained by

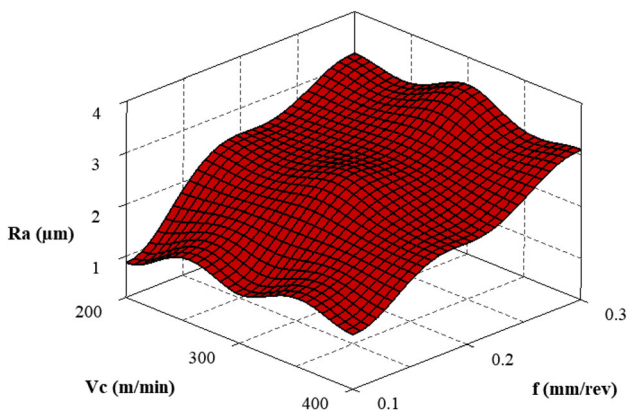

Figure 9. Ra assessment.

Figure 10. The spark formation.

the fact that the decrease in the strength of the chip due to the temperature increase at the tool-chip interface in the machining of the workpiece at high speeds, and as a result, the reduction of the chip adhering to the cutting tool [42]. On the other hand, an important consideration is the ductility of the workpiece material, and it is very significant in defining the surface roughness in the machining of the workpiece.

In the experiments carried out under dry cutting conditions at 400 m/min (Vc), 0.3 mm/rev (*f*), and 1 mm (ap) in figure 10, the spark is observed at the end of the turning process. This situation can be associated with the increase in cutting force and cutting temperature due to increasing the chip cross-section with increasing the feed rate at high cutting speed. Polmear *et al* reported that magnesium usually is machined dry but, where very high cutting speeds are involved, and there is a possibility of igniting fine turnings, it may be necessary to employ a coolant [40].

3.6 *Temperature (T)*

In machining processes, the mechanical energy spent to perform the process is converted into heat, and a significant amount of heat energy is released [41]. This heat energy is affected by process parameters such as cutting speed, feed rate, and depth of cut. The cutting temperature increases with the increase in these process parameters. In Mg-Al binary alloys with high ductility and low melting temperature, it is necessary to prevent chip adhering to the tool rather than tool wear. Furthermore, the ignition of Mg alloys, which are likely to ignite at high temperatures, can be controlled by the cutting temperature. Figure 11 shows the variation of cutting temperatures. When figure 11 is examined, the cutting temperature gradually increases as the cutting speed increases by 50% and 100%. A similar effect has appeared with an increase in feed rate and depth of cut. The cutting temperatures between 160 and 262°C was observed in the cutting zone. The highest cutting

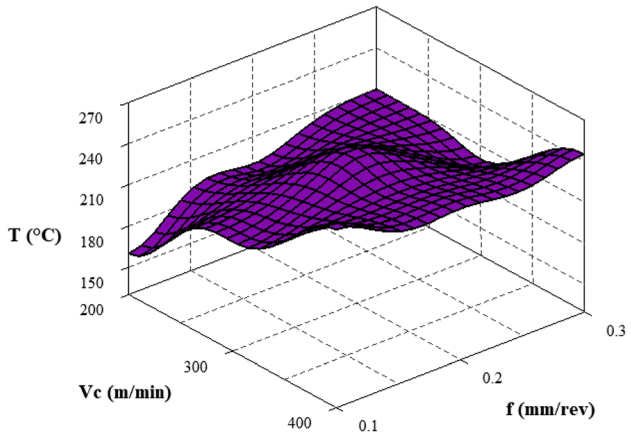

Figure 11. Cutting temperature assessment.

temperature was measured as 262°C at a cutting speed of 400 m/min and a feed rate of 0.3 and a depth of cut 2 mm, while the lowest cutting temperature was measured as 160°C at a cutting speed of 200 m/min and a feed rate of 0.1 and a depth of cut 1 mm. Dinesh *et al* reported that the cutting temperature increased with the increase of cutting speed and feed rate in the machining of ZK60, an Mg alloy, and the highest temperature was measured as 138 °C at 120 m/min and 0.15 mm/rev [42].

3.7 *Numerical analysis results*

In evaluating the numerical analysis results, Fc values, which are of primary importance in terms of energy consumption in the turning process, were used [43]. Experimental and simulation results were compared according to this important machinability output. It is observed that both experimental and numerical Fc values have a similar tendency with a percentage of 4.5% difference. As can be derived from figure 12, the Fc values increased with increasing feed rate and depth of cut, while the Fc was slightly decreased with increasing cutting speed. For example, The Fc values have about a 43% increase with a 200% increase of the *f* (mm/rev) while this increased rate is about 25% by the 100% increase of the *f* (mm/rev). This increasing trend in cutting force is similar for each depth of cut. The Fc values have average 16% increase with increasing ap as 100%, while average10% increase by increasing ap as 50%. This situation can be associated with the tool-chip contact area and the volume of material removed increases and resulting in the Fc increases [28, 44]. Nevertheless, there is a decreasing trend in Fc with the increase in cutting speed, but as also seen in the analysis of variance, the cutting speed is not very effective. This situation can be caused by the fact that BUE formation continues at high cutting speeds as a result of the ineffective cooling due to the fact that the experiments were carried out under dry cutting conditions. The lowest experimental Fc value was obtained with the feed rate of 0.1 mm/rev, the cutting speed of 400 m/min, and the depth of cut of 2 mm while the lowest simulation Fc value was obtained with the feed rate of 0.1 mm/rev, the cutting speed of 400 m/min, and the depth of cut of 1 mm. There is a 12% deviation between the Fc values obtained under these cutting conditions. The tool-workpiece interface friction coefficient and the Johnson-Cook model parameters used to define the workpiece material in the cutting simulation are thought to be effective on this deviation [31, 45]. The small deviations between the experimental and simulation results show that cutting force as well as important machinability outputs such as chip formation and tool wear, can be predicted by cutting simulations based on the finite element method.

3.8 *Optimization of all outputs (Fc, Fp, Ff, Ra, and T)*

Variance analysis was used to find the significance level of the factors on all outputs, while used S/N response to be determining the ideal levels of the factors. Anova results for all outputs and the S/N response and are given in Tables 7 and 8, respectively. When Tables 7 and 8 are examined, it is seen that the most significant factor on the Fc, Fp, F*f* and Ra is f (mm/rev) and this is followed by Vc (m/min) and a (mm), respectively, while the most significant factor on the T is Vc (m/min) with an additive rate of 70.83%. The optimal combination of process parameters for the cutting force components are determined as (A) 400 m/min, (B) 0.1 mm/rev, and (C) 2 mm. In tests performed on these parameters, the Fc, Fp, and F*f* values are measured as 23.437 N, 3.421 N, and 4.686 N, respectively. The optimal combination of process parameters for Ra are also determined as (A) 400 m/min, (B) 0.1 mm/rev, and (C) 1 mm.

As a result, the lowest Ra value is achieved as 0.85 µm in tests performed on these parameters. Finally, the optimal combination of process parameters for T are determined as (A) 200 m/min, (B) 0.1 mm/rev, and (C) 1 mm. the lowest T value is obtained as 160°C in tests performed on these parameters.

3.9 *Multi-response optimization using grey relational analysis (GRA)*

The Taguchi method is a stand-alone method for optimizing the performance response. Multi-criteria decision-making methods are used together with the Taguchi method to transform multiple performance responses into a single-response optimization problem. Gray relationship analysis, which is one of these methods, is widely used to solve multiobjective decision-making problems in the machining industry [46, 47]. In this study, it is used to simultaneously identify an optimal combination of process parameters

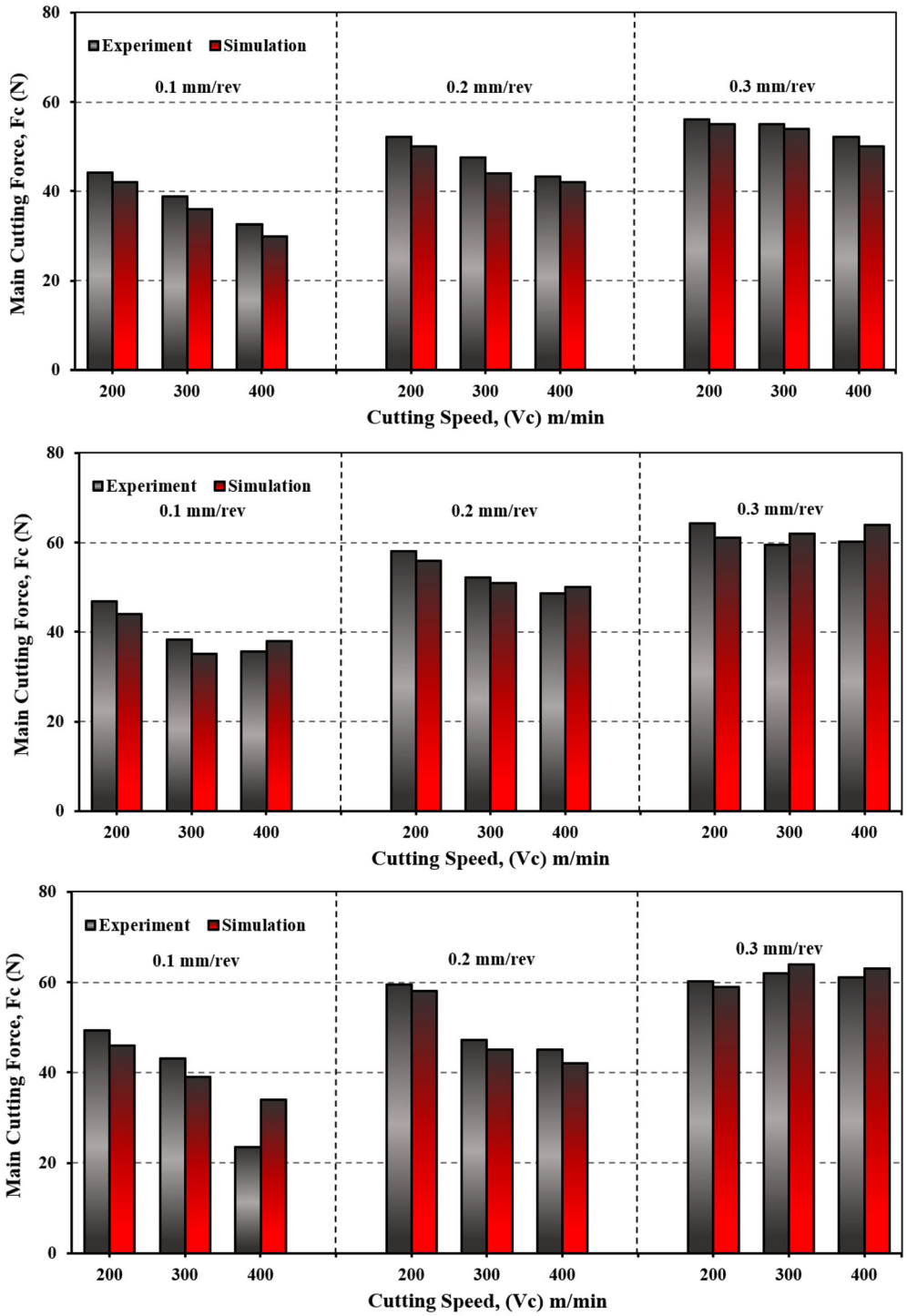

Figure 12. Comparison of experiment and simulation results for Fc.

according to the multiple performance characteristics (Ra, T and F). Firstly, experimental data were normalized between '0' and '1'. The gray correlation coefficient was calculated for the normalized multiple performance characteristics. Then, the gray relational grade (GRG) was calculated by averaging the GRA coefficient. Normalized data, gray correlation coefficients, GRA coefficient values and S/N ratios for each experimental set are given in Table 9. In Table 9, the average value of the gray coefficients from each performance characteristic gives the degree of gray relations for each experimental set, and as a result, the combination with the highest GRG value shows a

Table 7. Result of variance for all outputs.

Source	Degree of freedom (DoF)	Sum of squares (SS)	Mean square (MS)	F ratio	P ratio	Contribution rate (%)
Fc						
Vc (m/min)	2	214.74	107.37	5.81	0.147	18.18
f (mm/rev)	2	819.96	409.98	22.17	0.043	69.43
a (mm)	2	109.24	54.62	2.95	0.253	9.25
Error	2	36.99	18.49			3.13
Total	8	1180.93				100
Fp						
Vc (m/min)	2	0.45509	0.22754	4.64	0.177	5.88
f (mm/rev)	2	6.97059	3.48529	71.06	0.014	90.04
a (mm)	2	0.21775	0.10888	2.22	0.311	2.81
Error	2	0.09810	0.04905			1.27
Total	8	7.74152				100
Ff						
Vc (m/min)	2	5.1541	2.5771	16.16	0.058	10.25
f (mm/rev)	2	44.5001	22.2500	139.49	0.007	88.53
a (mm)	2	0.2929	0.1465	0.92	0.521	0.58
Error	2	0.3190	0.1595			0.63
Total	8	50.2662				100
Ra						
Vc (m/min)	2	0.17387	0.08693	3.84	0.207	2.73
f (mm/rev)	2	6.12007	3.06003	135.20	0.007	96.22
a (mm)	2	0.02160	0.01080	0.48	0.677	0.34
Error	2	0.04527	0.02263			0.71
Total	8	6.36080				100
T						
Vc (m/min)	2	5705.56	2852.78	146.71	0.007	70.83
f (mm/rev)	2	272.22	136.11	7	0.125	3.38
a (mm)	2	2038.89	1019.44	52.43	0.019	25.31
Error	2	38.89	19.44			0.48
Total	8	8055.56				100

Table 8. S/N response of all outputs.

	Cutting factors					
	A (Vc)	B (*f*)	C (*a*)	A (Vc)	B (*f*)	C (a)
Fc				*Ff*		
1	− 34.57	− **30.62**	− 33.45	− 19.38	− **14.73**	− 18.28
2	− 33.28	− 33.79	− 34.14	− 17.79	− 19.24	− 18.41
3	− **31.88**	− 35.31	− **32.13**	− **17.48**	− 20.67	− **17.96**
Delta	2.69	4.69	2.01	1.9	5.94	0.45
Fp				*Ra*		
1	− 13.86	− **11.89**	− 13.41	− 6.391	− **1.894**	− **6.211**
2	− 14.06	− 13.34	− 14.08	− 7.336	− 7.748	− 6.798
3	− **12.96**	− 15.66	− **13.39**	− **6.152**	− 10.237	− 6.870
Delta	1.11	3.77	0.69	1.185	8.342	0.658
T						
1	− **45.37**	− **46.28**	− **45.90**			
2	− 46.69	− 46.93	− 46.60			
3	− 47.90	− 46.75	− 47.45			
Delta	2.53	0.65	1.55			

Table 9. Gray relational analysis results.

	Experimental results			Normalize values			Gray relational coefficient					
	Ra	T	F	Ra	T	F	Ra	T	F	GRG	S/N ration	Order
1	1.14	160	34.43	1.000	1.000	0.325	1.000	1.000	0.425	0.808	− 1.851	1
2	2.50	190	53.89	0.416	0.700	0.744	0.461	0.625	0.662	0.543	− 5.304	4
3	3.19	210	65.74	0.120	0.500	1.000	0.362	0.500	1.000	0.431	− 7.310	7
4	1.35	210	29.53	0.910	0.500	0.219	0.847	0.500	0.390	0.674	− 3.426	2
5	2.69	240	45.45	0.335	0.200	0.562	0.429	0.385	0.533	0.407	− 7.808	8
6	3.47	200	57.46	0.000	0.600	0.821	0.333	0.556	0.737	0.444	− 7.052	6
7	1.25	260	19.38	0.953	0.000	0.000	0.914	0.333	0.333	0.624	− 4.096	3
8	2.16	240	38.95	0.562	0.200	0.422	0.533	0.385	0.464	0.459	− 6.763	5
9	3.10	245	62.68	0.159	0.150	0.934	0.373	0.370	0.883	0.372	− 8.589	9

Table 10. Answer table for GRG.

	Grey Relational Grade				
Code	Level 1	Level 2	Level 3	Delta	Rank
A	**0.5940**	0.5083	0.4850	0.1090	2
B	**0.7020**	0.4697	0.4157	0.2863	1
C	**0.5703**	0.5297	0.4873	0.0830	3

Average of total gray relationship grade = 0.529

strong correlation between the normalization values and the experimental results [31]. The optimum combination for process parameters is $A_1B_1C_1$ as experimental set 1 has the highest GRG coefficient value. This situation is also confirmed in the S/N response results for the GRG (Table 10). The total GRG average for 9 experiments was calculated as 0.529.

Moreover, ANOVA was applied to determine the effects of process parameters on multiple performance characteristics. The feed rate is the most effective parameter on multiple performance characteristics the ANOVA results shown in Table 11. Table 12 summarizes the optimum process parameters obtained using the Taguchi-based gray relational analysis in turning of AZ 91 alloy.

Table 12. Optimum levels of process conditions for output parameters.

Output parameter	Analysis method	Optimal process factors
Ra	Taguchi	A3B1C1
T	Taguchi	A1B1C1
F	Taguchi	A3B1C3
Ra, T and F	Grey relational analysis	A1B1C1

3.9.1 *Mathematical modeling of all outputs (Fc, Fp, Ff, Ra, and T)* The correlations between input factors and output parameters (Fc, Fp, Ff, Ra and T) were expressed using linear and quadratic regressions. The final response equations derived for all outputs and determination coefficients are given in Table 13. Furthermore, figure 13 shows the comparison of experimental results and estimated values obtained by quadratic regression analysis for all outputs.

As can be deduced in Table 13, the high (R^2) values of second-degree models compared to linear models indicate that second-degree models are more successful in

Table 11. Result of variance for the output parameters.

Factors	Degree of freedom (DoF)	Sum of squares (SS)	Mean square (MS)	F ratio	P ratio	Contribution rate (%)
GRG						
Vc	2	0.019764	0.009882	53.67	0.018	11.67
f	2	0.138882	0.069441	377.17	0.003	82.01
ap	2	0.010335	0.005167	28.07	0.034	6.10
Error	2	0.000368	0.000184			0.22
Total	8	0.169349				100

Table 13. Developed equations for the output parameters.

Factor	Equation	R^2 (%)
Fc	$Fc_t = 48 - 0.0593Vc + 115.9f - 3.85ap$	88.03
	$Fc_q = 23.67 - 0.1343Vc + 84.71f + 50.39ap + 0.000019Vc^2 - 183.3f^2 - 16.67ap^2 + 0.3638Vcf - 0.006084Vcap$	99.15
Fp	$Fp_t = 3.337 - 0.00212Vc + 10.58f + 0.048ap$	90.31
	$Fp_q = 0.1313 + 0.02086Vc - 10.31f + 2.643ap - 0.000042Vc^2 + 42.52f^2 - 0.7987ap^2 + 0.01433Vcf - 0.00056Vcap$	99.8
Ff	$Ff_t = 5.46 - 0.00834Vc + 26.58f + 0.158ap$	92.71
	$Ff_q = 7.671 - 0.05145Vc + 55.2f + 2.191ap + 0.000061Vc^2 - 97.38f^2 - 0.5447ap^2 + 0.03552Vcf - 0.000437Vcap$	99.9
Ra	$Ra_t = 0.29 - 0.000533Vc + 10.033f + 0.12ap$	95.57
	$Ra_q = -1.895 + 0.006067Vc + 19.72f + 0.6727ap - 0.000014Vc^2 - 28.67f^2 - 0.1933ap^2 + 0.0042Vcf + 0.000693Vcap$	99.7
T	$T_t = 61.4 + 0.3083Vc + 41.7f + 36.67ap$	97.14
	$T_q = 19.33 + 0.525Vc + 481.7f + 3.667ap - 0.000183Vc^2 - 750f^2 + 10ap^2 - 0.4333Vcf - 0.01333Vcap$	99.87

estimating output parameters. Furthermore, As can be seen figure 13, the experimental and estimated values are very close to each other.

3.9.2 *Confirmation tests* After expressing the relationship between inputs and outputs in the optimization process mathematically, its accuracy should be tested.

At this stage, Eqs. (3), (4), (5), (6), and (7) have been used, respectively, to calculate Fc, Fp, F*f*, Ra, and T values according to the optimal combination of process parameters determined by the Taguchi method.

$$Fc_{opt} = (A_3 - T_{Fc}) + (B_1 - T_{Fc}) + (C_3 - T_{Fc}) + T_{Fc} \quad (3)$$

$$Fp_{opt} = (A_3 - T_{Fp}) + (B_1 - T_{Fp}) + (C_3 - T_{Fp}) + T_{Fp} \quad (4)$$

$$Ff_{opt} = (A_3 - T_{Ff}) + (B_1 - T_{Ff}) + (C_3 - T_{Ff}) + T_{Ff} \quad (5)$$

$$Ra_{opt} = (A_3 - T_{Ra}) + (B_1 - T_{Ra}) + (C_1 - T_{Ra}) + T_{Ra} \quad (6)$$

$$T_{opt} = (A_1 - T_T) + (B_1 - T_T) + (C_1 - T_T) + T_T \quad (7)$$

$T_{Fc}(47.604), T_{Fp}(4.89), T_{Ff}(8.512), T_{Ra}(2.263)$, and$T_T$ (217.222) values are the mean of the total experiment for each output parameter. Consequently, The Fc, F*f*, Fp, Ra, and T values have been calculated to be 25.572N, 3.552N, 4.871N, 0.915 μm, and 162.256°C, respectively. The confidence interval (CI) was calculated using the Eqs. (8) and (9). For equation (8), $F_{0.05,1,2}$=18.512 (from F test table), $Ve_{Fc} = 18.49$, $Ve_{Ff} = 0.1595$, $Ve_{Fp} = 0.04905$, $Ve_{Ra} = 0.02263$, and $Ve_T = 19.44$ [Table 5], $R = 1$, $N = 9$, $T_{dof} = 6$ and $n_{eff} = 2.571$ (Eq. (15)).

$$CI = \sqrt{F_{a,1,fe} V_e \left[\frac{1}{n_{eff}} + \frac{1}{R}\right]} \quad (8)$$

$$n_{eff} = \frac{N}{1 + T_{dof}} \quad (9)$$

$CI_{Fc}, CI_{Fp}, CI_{Ff}, CI_{Ra}$, and$CI_T$ obtained as 5.067, 1.123, 2.025, 1.118, and 22.35 by using Eq. (8), respectively.

$$\begin{aligned}&[Fc_{opt} - CI_{Fc}] < Fc_{exp} < [Fc_{opt} + CI_{Fc}]\\ &= 25.572 - 5.067 < 23.437 < [25.572 + 5.067]\\ &= 20.505 < 23.437 < 30.639\end{aligned} \quad (10)$$

$$\begin{aligned}&[Fp_{opt} - CI_{Fp}] < Fp_{exp} < [Fp_{opt} + CI_{Fp}]\\ &= 3.552 - 1.123 < 3.42 < [3.552 + 1.123]\\ &= 2.429 < 3.42 < 4.675\end{aligned} \quad (11)$$

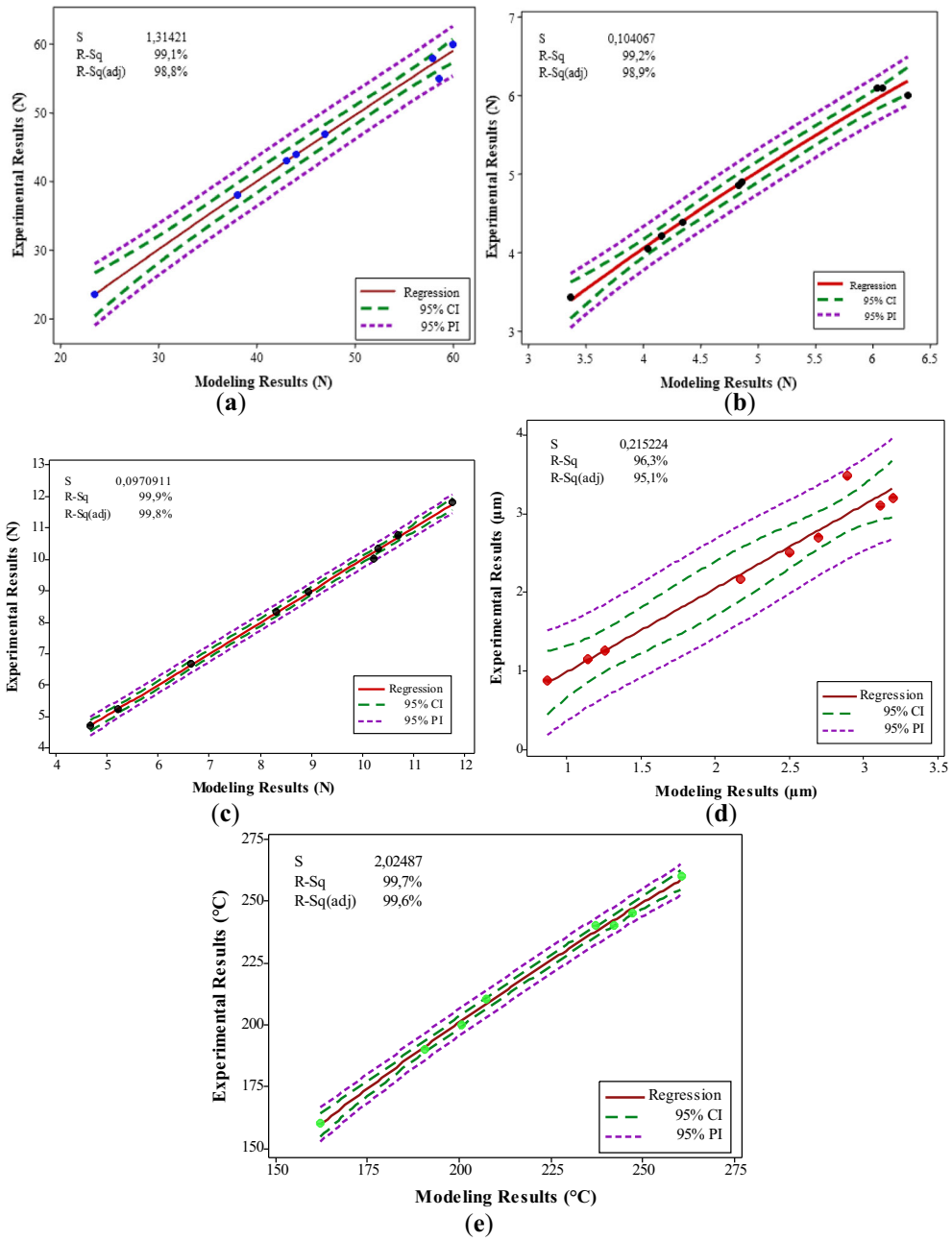

Figure 13. The comparison of experimental and modeling results for all outputs a) Fc, b) Fp, c) F*f*, d) Ra, and e) T.

$$\begin{aligned}&\left[Ff_{opt}-CI_{Ff}\right]<Ff_{exp}<\left[Ff_{opt}+CI_{Ff}\right]\\&=4.872-2.025<4.686<[4.871+2.025]\\&=2.847<4.686<6.896\end{aligned}\tag{12}$$

$$\begin{aligned}&\left[Ra_{opt}-CI_{Ra}\right]<Ra_{exp}<\left[Ra_{opt}+CI_{Ra}\right]\\&=0.915-1.118<0.85<[0.915+1.118]\\&=-0.203<0.85<2.032\end{aligned}\tag{13}$$

$$\begin{aligned}&\left[T_{opt}-CI_{T}\right]<T_{exp}<\left[T_{opt}+CI_{T}\right]\\&=162.256-22.35<160<[162.256+22.35]\\&=139.906<160<184.606\end{aligned}\tag{14}$$

According to Eqs. (10), (11), (12), (13), and (14), it was showed that all outputs are within the confidence interval limit, respectively. Consequently, the optimization process is successfully performed with Taguchi method at 95% significance level. Figure 14 shows the validation interval

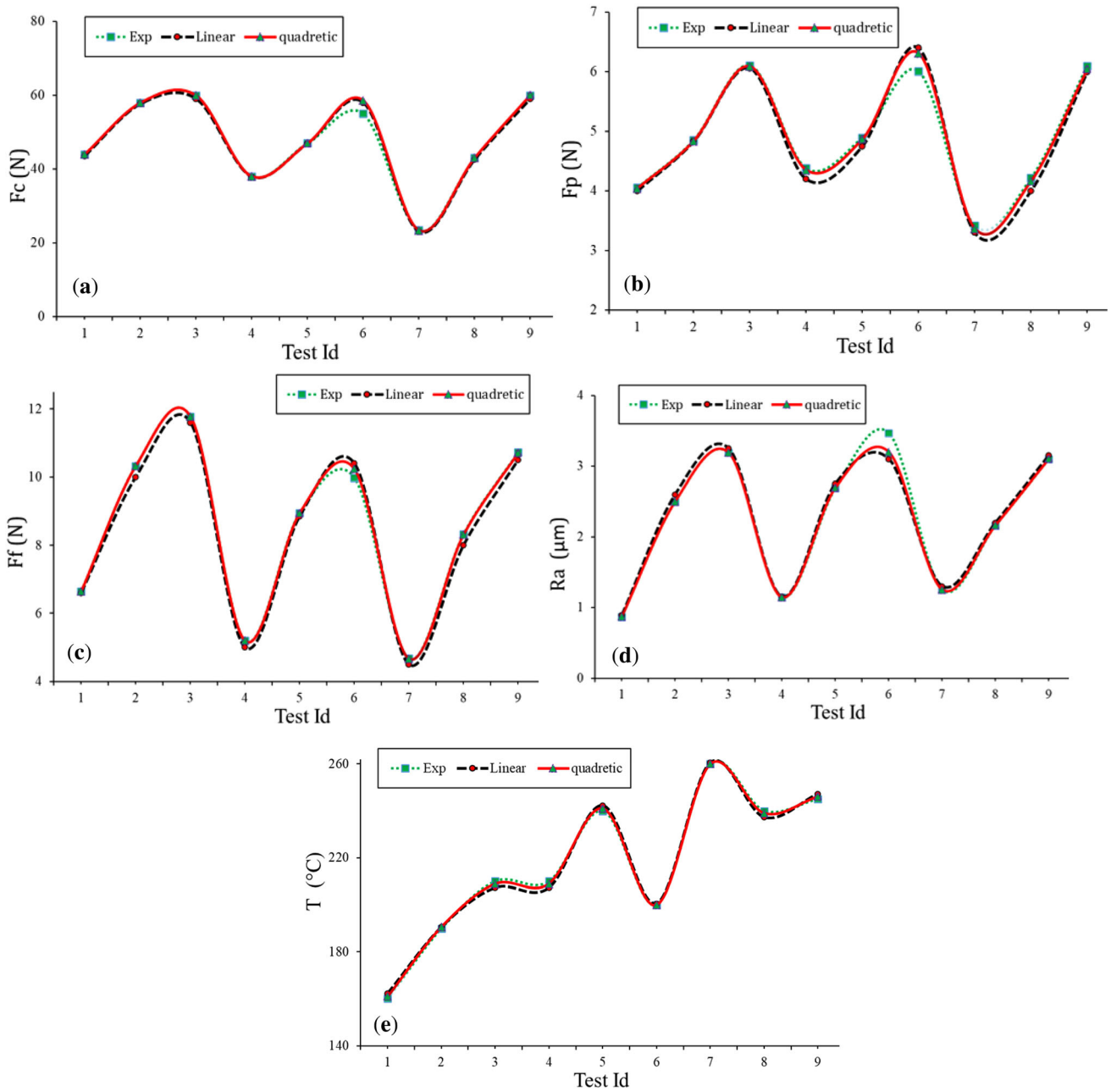

Figure 14. Comparison graph of the experimental measured and predicted values for Fc (a), Fp (b), Ff (c), Ra (d), and T (e).

for each experimental level group of the mathematical equations developed for all outputs. Furthermore, the validation results for all outputs are given in Table 14. From Table xx6, the optimal combination of process parameters for the cutting force components (Fc, Fp, Ff), Ra and T is found to be: A3B1C2, A3B1C1, and A1B1C1, respectively. The symbols A, B, and C represents process parameters: Vc, *f*, and ap respectively, and numbers represents the levels. On the other hand, the random combination of process parameters for all outputs has been chosen to be: A1B2C1. This means, Vc is 200 m/min, *f* is 0.2 mm/rev, and ap is 1 mm.

According to figure 14 and Table 14, the results produced by the mathematical equations developed to estimate the outputs are within the error limits compared with the actual results. Moreover, Günay reported that error values should be less than 20 percent for reliable statistical analysis [48]. As a result, it is noticeable that the estimation

Table 14. The verification test results.

	Linear regression equations			Quadratic regression equations		
Level	Exp.	Pred.	Error (%)	Exp.	Pred.	Error (%)
Fc (N)						
$A_3B_1C_3$	23.43	27.67	18.06	23.43	23.41	0.08
$A_1B_2C_1$	54.15	55.47	2.43	54.15	54.23	0.14
Fp (N)						
$A_3B_1C_3$	3.42	3.64	6.43	3.42	3.36	0.29
$A_1B_2C_1$	4.45	5.07	13.93	4.45	4.56	2.47
Ff (N)						
$A_3B_1C_3$	4.68	5.09	8.76	4.68	4.67	0.21
$A_1B_2C_1$	9.85	9.26	5.98	9.85	9.94	0.91
Ra (μm)						
$A_3B_1C_1$	0.85	1.10	29.41	0.85	0.90	5.88
$A_1B_2C_1$	2.05	2.31	12.68	2.05	2.25	9.75
T (°C)						
$A_1B_1C_1$	160.00	163.90	2.43	160.00	160.00	0.00
$A_1B_2C_1$	175.45	168.07	4.20	175.45	177.01	0.89

equations give successful results with the high coefficients of determination (R^2) values and within the confidence interval in the confirmation test results.

4. Conclusions

The present work focuses on the experimental and statistical analysis of the influence of process parameters on the Fc, Fp, F*f*, Ra, and T in machining of AZ91 Mg alloy produced by the casting method. Some key results from this work can be itemized as follows;

- α-Mg phase and β-intermetallic ($Mg_{17}Al_{12}$) phase were observed in the microstructure of the AZ91 alloy produced by the casting method.
- The hardness of the produced sample was measured as 58.24±5 HV.
- According to the S/N ratios, the optimal combination of process parameters for the lowest cutting force components are A3B1C3 (cutting speed 400 m/min, feed rate 0.1 mm/rev, and depth of cut 2 mm). The Fc, Fp, and F*f* values are measured as 23.43 N, 3.42 N, and 4.68 N in the turning experiment performed in these parameters, respectively.
- In the tool wear examination, the tendency of built-up edge (BUE) formation that change the cutting tool geometry was observed.
- The spark was observed at the end of the turning operation performed at a cutting speed of 400 m/min and a feed rate of 0.3 mm/rev, and a depth of cut of 1 mm.
- In the machining of AZ91 Mg alloy, it is necessary to prevent the chip from adhering to the tool rather than the tool wear.
- Generally, with the increase in feed rate, a significant increase has been shown in the surface roughness (Ra) and the cutting force values.
- The optimal combination of process parameters for the lowest Ra are A3B1C1 (cutting speed 400 m/min, feed rate 0.1 mm/rev, and depth of cut 1 mm). The Ra value is measured as 0.85 μm in the turning experiment performed in these parameters.
- The optimal combination of process parameters for the lowest T are A1B1C1 (cutting speed 200 m/min, feed rate 0.1 mm/rev, and depth of cut 1 mm). The T value is measured as 160°C in the turning experiment performed in these parameters.
- According to the ANOVA results obtained after Taguchi-based gray relational analysis, the feed rate is the most effective parameter on multiple performance characteristics.
- According to the grey correlation analysis results, A1B1C1 (i.e., cutting speed=200 m/min, feed rate=0.1 mm/rev, dept of cut= 1 mm,) is the optimum process parameter for multiple performance characteristics.
- It was found that there is an average of 4.5% deviation between the experimental and simulation results of Fc.
- The developed linear and quadratic models show an excellent bond between the test and predicted values for Fc, Ff, Fp, Ra and T with high correlation coefficients and within the confidence interval of 95 per cent.

References

[1] Mordike B L and Ebert T 2001 Magnesium properties applications potential. *Mater. Sci. Eng. A.* 302: 37–45

[2] Buldum B, Şik A and Özkul I 2012 Investigation of magnesium alloys machinability. *Int. J. Elect. Mech. Mechat. Eng.* 2(3): 261–268
[3] Shi K, Zhang D and Ren J 2015 Optimization of process parameters for surface roughness and microhardness in dry milling of magnesium alloy using Taguchi with grey relational analysis. *Int. J. Adv. Manuf. Technol.* 81(1): 645–651
[4] Akyuz B 2014 Effects of Si and Zn on machinability and wear resistance of AZ91 and AS91 magnesium alloys. *Mater. Test.* 56(9): 703–708
[5] Tönshoff H K and Winkler J 1997 The influence of tool coatings in machining of magnesium. *Surf. Coat. Technol.* 94: 610–616
[6] Akyuz B 2014 Comparison of the machinability and wear properties of magnesium alloys. *Int. J. Adv. Manuf. Technol.* 75(9–12): 1735–1742
[7] Öztürk F and Kaçar I 2012 Investigation of magnesium alloys and their applications. *NOHU. J. Eng. Sci.* 1(2): 12–20
[8] Aghion E, Bronfin B and Eliezer D 2001 The role of the magnesium industry in protecting the environment. *J. Mater. Process. Technol.* 117(3): 381–385
[9] Staiger M P, Pietak A M, Huadmai J and Dias G 2006 Magnesium and its alloys as orthopedic biomaterials: a review. *Biomaterials* 27(9): 1728–1734
[10] Gariboldi E 2003 Drilling a magnesium alloy using PVD coated twist drills. *J Mater. Process. Technol.* 134(3): 287–295
[11] Shi K, Ren J, Zhang D, Zhai Z and Huang X 2017 Tool wear behaviors and its effect on machinability in dry high-speed milling of magnesium alloy. *J. Adv. Manuf. Technol.* 90(9): 3265–3273
[12] Hou J Z, Zhou W and Zhao N 2010 Effect of cutting parameters on ignition of AM50A Mg alloy during face milling. *Mater. Manuf. Process.* 25(10): 1048–1051
[13] Şirin Ş, Yıldırım Ç V, Kıvak T and Sarıkaya M 2021 Performance of cryogenically treated carbide inserts under sustainable cryo-lubrication assisted milling of Inconel X750 alloy. *Sustain. Mater. Technol* 29: e00314
[14] Esfe M H, Bahiraei M and Mir A 2020 Application of conventional and hybrid nanofluids in different machining processes: a critical review. *Adv. Colloid Interface Sci.* 282: 102199
[15] Hou J, Zhao N and Zhu S 2011 Influence of cutting speed on flank temperature during face milling of magnesium alloy. *Mater. Manuf. Process.* 26(8): 1059–1063
[16] Aslan D and Budak E 2014 Semi-analytical force model for grinding operations. *Procedia CIRP* 14: 7–12
[17] Kayir Y 2014 Optimization of the cutting parameters for drilling magnesium alloy AZ91. *Mater. Test.* 56(1): 47–53
[18] Vasu C, Andhare A B and Dumpala R 2021 Multiobjective optimization of performance characteristics in turning of AZ91 mg alloy using grey relational analysis *Mater. Today Proc.* 42: 642–649
[19] Shi K, Ren J, Zhang D, Zhai Z and Huang X 2017 Tool wear behaviors and its effect on machinability in dry high-speed milling of magnesium alloy. *Int. J. Adv. Manuf. Technol.* 90(9): 3265–3273
[20] Dey A, Debnath S and Pandey K M 2017 Optimization of electrical discharge machining process parameters for Al6061/Cenosphere composite using grey-based hybrid approach. *T. Nonferr. Met. Soc.* 27(5): 998–1010
[21] Akyuz B 2013 Influence of Al content on machinability of AZ series mg alloys. *T. Nonferr. Met. Soc.* 23(8): 2243–2249
[22] Chowdary S, Dumpala R and Kondaiah V V 2018 Influence of heat treatment on the machinability and corrosion behavior of AZ91 Mg alloy. *J. Magn. Alloys.* 6(1): 52–58
[23] Çiçek B, Ahlatçı H and Sun Y 2013 Wear behaviours of Pb added Mg–Al–Si composites reinforced with in situ Mg2Si particles. *Mater. Des.* 50: 929–935
[24] Nas E and Altan N 2020 Optimization of the machining parameters in turning of hardened hot work tool steel using cryogenically treated tools. *Surf. Rev. Lett.* 27(05): 1950177
[25] Sharma A, Singh R C and Singari R M 2020 Optimization of machining parameters during cryogenic turning of AISI D3 steel. *Sādhanā* 45: 124
[26] Akgün M and Demir H 2021 Optimization of cutting parameters affecting surface roughness in turning of Inconel 625 superalloy by cryogenically treated tungsten carbide inserts. *SN Appl. Sci.* 3: 277
[27] Kalyon A 2020 Optimization of machining parameters in sinking electrical discharge machine of caldie plastic mold tool steel. *Sādhanā.* 45: 65
[28] Korkmaz M E and Günay M 2018 Finite element modelling of cutting forces and power consumption in turning of AISI 420 martensitic stainless steel. *Arab. J. Sci. Eng.* 43(9): 4863–4870
[29] Bagheri B, Abdollahzadeh A, Abbasi M and Kokabi A H 2021 Effect of vibration on machining and mechanical properties of AZ91 alloy during FSP: modeling and experiments. *Int. J. Mater. Form.* 14(4): 623–640
[30] Zhou X, Zhao C M, Li L and Huang H J 2014 Numerical simulation of dynamic behavior of extruded AZ91D magnesium alloy based on SHPB experiment. *Chin. J. Nonferr. Metal.* 24(8): 1968–1975
[31] Yaşar N 2019 Thrust force modelling and surface roughness optimization in drilling of AA-7075: FEM and GRA. *J. Mech. Sci. Technol.* 33(10): 4771–4781
[32] Kerenciler H, Gündüz S, Erden M A, Türkmen M and Karabulut H 2016 Effect of aging on the microstructure and mechanical properties of magnesium alloy AZ31. *Met. Sci. Heat Treat.* 58(3): 179–184
[33] Fu X Y, Jia R L, Ding Y F, Gong T H, Ma W and Guo F 2022 Effect of hot extrusion on AZ91 alloy corrosion behaviour. *Corros. Eng. Sci. Technol.* 57(2): 140–146
[34] Gassama B, Ozden G and Oteyaka M O 2022 The effect of deep cryogenic treatment on the wear properties of AZ91 magnesium alloy in dry and in 0.9 wt% NaCl medium. *Sādhanā.* 47(1): 15
[35] Liang S M, Chena R S, Blandin J J, Suery M and Han E H 2008 Thermal analysis and solidification pathways of Mg–Al–Ca system alloys. *Mater. Sci. Eng., A.* 480: 365-372
[36] Floriano R, Leiva D R, Melo G C, Ishikawa T T, Huot J, Kaufman M, Figueroa S J A, Mendoza-Zelis L A, Damonte L C and Botta W J 2017 Low temperature rolling of AZ91 alloy for hydrogen storage. *Int. J. Hydrogen Energy* 42(49): 29394–29405
[37] Ciftci I 2006 Machining of austenitic stainless steels using CVD multi-layer coated cemented carbide tools. *Tribol. Int.* 39(6): 565–569

[38] Özlü B 2021 Investigation of the effect of cutting parameters on cutting force, surface roughness and chip shape in turning of Sleipner cold work tool steel. *J. Fac. Eng. Archit. Gazi Univ.* 36(3): 1241–1251

[39] Demir H and Gündüz S 2009 The effects of aging on machinability of 6061 aluminium alloy. *Mater. Des.* 30: 1480–1483

[40] Demir H, Gündüz S and Erden M A 2018 Influence of the heat treatment on the microstructure and machinability of AISI H13 hot work tool steel. *Int. J. Adv. Manuf. Technol.* 95(5): 2951–2958

[41] Boothroyd G and Knight W A 2005 *Fundamentals of metal machining and machine tools. London*: 3rd Ed., CRC Press. p. 50–180

[42] Polmear I J 1994 Magnesium alloys and applications. *Mater. Sci. Technol.* 10(1): 1–16

[43] Danish M 2020 Chapter *10-high speed machining of magnesium and its alloys.* High Speed Machining. Academic, London, p. 263–279

[44] Dinesh S, Senthilkumar V, Asokan P and Arulkirubakaran D 2015 Effect of cryogenic cooling on machinability and surface quality of bio-degradable ZK60 Mg alloy. *Mater. Des.* 87: 1030–1036

[45] Korkmaz M E, Yaşar N and Günay M 2020 Numerical and experimental investigation of cutting forces in turning of Nimonic 80A superalloy. *Eng. Sci. Technol. Int. J.* 23(3): 664–673

[46] Thrinadh J, Mohapatra A, Datta S and Masanta M 2020 Machining behavior of Inconel 718 superalloy: Effects of cutting speed and depth of cut. *Mater. Today Proc.* 26: 200–208

[47] Özel T 2006 The influence of friction models on finite element simulations of machining. *Int. J. Mach. Tools Manuf.* 46(5): 518–530

[48] Kumar R, Bilga P S and Singh S 2017 Multi objective optimization using different methods of assigning weights to energy consumption responses, surface roughness and material removal rate during rough turning operation. *J. Clean. Prod.* 164: 45–57

[49] Iç Y T, Yurdakul M, Dengiz B and Şaşmaz T 2023 Investigation of the importance of machine sequence flexibility on a flexible manufacturing system performance. *GU J. Sci.* 36(2): 735–750

[50] Günay M and Meral T 2020 Modelling and multiresponse optimization for minimizing burr height, thrust force and surface roughness in drilling of ferritic stainless steel. *Sādhanā* 45: 273